Spatiotemporal Switches in Progenitor Cell Fate Govern Upper Hair Follicle Growth and Maintenance

Marianne S. Andersen[1,8], Svetlana Ulyanchenko[2,8], Pawel J. Schweiger[2], Edouard Hannezo[3], Benjamin D. Simons[4,5,6] and Kim B. Jensen[2,7]

Journal of Investigative Dermatology (2025) **145,** 2191–2202; doi:10.1016/j.jid.2025.01.034

The epidermis provides a protective barrier against hostile environments. However, our knowledge of how this barrier forms during development and is subsequently maintained remains incomplete. The infundibulum is a cylindrical epidermal tissue compartment that serves as an outlet for hair follicles protruding from the skin and the excretion of the sebaceous glands that are essential for proper skin function. In this study, we applied quantitative fate mapping to address how infundibulum are maintained during adulthood. We demonstrate that progenitors build and maintain tissues through stochastic cell fate choices. Long-term analysis identified a preferential transient contribution from cells initially located at the bottom of the structure to the maintenance of the tissue, with bursts of local progenitor expansion associated with the phases of hair growth. Beyond providing compartment-wide insights into progenitor cell dynamics in infundibulum, these findings demonstrate how spatiotemporal regulation controls transient progenitor dominance.

Keywords: Epidermis, Infundibulum, Quantitative fate mapping, Skin, Stem cells

INTRODUCTION

Similar to many epithelial tissues, the skin epidermis is maintained by specialized proliferative stem cells or progenitors that can either self-renew through cell duplication or differentiate into more specialized postmitotic cells that support tissue function. Throughout life, balanced cell-fate decisions within the epidermis provide the basis for constant tissue renewal and maintenance. Epidermal stem cells are in contact with the basement membranes. As the cells differentiate, they lose their attachment and move toward the skin surface (Fuchs, 2008). The epidermis consists of different components: the outer layer, the interfollicular epidermis (IFE), which forms a protective shield against hostile environments, and adnexal structures such as the pilosebaceous unit, which provides auxiliary functions such as insulation and lubrication. Pilosebaceous unit functions are executed by distinct compartments such as the hair follicle (HF), which gives rise to hair growth (Plikus et al, 2008), and the sebaceous gland (SG), which is the source of sebum production (Ehrmann and Schneider, 2016; Zouboulis et al, 2016). These parts are joined by the infundibulum (INF), which forms an essential funnel that supports both functions. In homeostasis, each of these compartments (HF, SG, INF) are maintained as independent units by specialized stem cells (Page et al, 2013). However, the mechanism underlying the cellular replenishment of the INF remains unclear.

During development, pilosebaceous unit formation is initiated within the expanding IFE as HF placodes elongate into the underlying dermis. The cellular position within the forming placode, which is associated with specific marker expression, governs the fate of individual cells (Morita et al, 2021). During this process, lineage-committed epidermal cells expressing *Lrig1* give rise to the SG and INF (Andersen et al, 2019; Jensen et al, 2009; Snippert et al, 2010). Quantitative fate mapping studies have shown that SG formation is achieved through an imbalance in cell fate decisions toward cell duplication, giving rise to progenitors that can continue to fuel tissue growth (Andersen et al, 2019). A similar behavioral pattern has been associated with the postnatal formation of the IFE (Clayton et al, 2007; Dekoninck et al, 2020; Mascré et al, 2012; Sada et al, 2016). Once the adult sizes of different compartments are reached, cell fate decisions are balanced to support tissue

[1]Biotech Research and Innovation Centre (BRIC), Faculty of Health and Medical Sciences, University of Copenhagen, Copenhagen, Denmark; [2]Novo Nordisk Foundation Center for Stem Cell Medicine, ReNEW, Faculty of Health and Medical Sciences, University of Copenhagen, Copenhagen, Denmark; [3]Institute of Science and Technology Austria, Klosterneuburg, Austria; [4]Centre for Mathematical Science, Department of Applied Mathematics and Theoretical Physics, University of Cambridge, Cambridge, United Kingdom; [5]The Wellcome Trust/Cancer Research UK Gurdon Institute, University of Cambridge, Cambridge, United Kingdom; [6]The Wellcome Trust/Medical Research Council Stem Cell Institute, University of Cambridge, Cambridge, United Kingdom; and [7]Department of Biomedical Sciences, Faculty of Health and Medical Sciences, University of Copenhagen, Copenhagen, Denmark

[8]These authors contributed equally to this work.

Correspondence: Edouard Hannezo, Institute of Science and Technology Austria, Am Campus 1, Klosterneuburg A-3400, Austria. E-mail: Edouard.Hannezo@ist.ac.at and Kim B. Jensen, Novo Nordisk Foundation Center for Stem Cell Medicine (ReNEW), Faculty of Health and Medical Sciences, University of Copenhagen, Blegdamsvej 3B, Copenhagen DK-2200, Denmark. E-mail: kim.jensen@sund.ku.dk

Abbreviations: 4-OHT, 4-hydroxy tamoxifen; EdU, 5-ethynyl-2′-deoxyuridine; HF, hair follicle; IFE, interfollicular epidermis; INF, infundibulum; SG, sebaceous gland

Received 12 December 2023; revised 21 January 2025; accepted 26 January 2025; accepted manuscript published online 24 February 2025; corrected proof published online 22 March 2025

maintenance. Throughout life, the lower portion of the HF dedicated to hair growth moves episodically through distinct phases of turnover, beginning with expansion (anagen) to support HF formation, regression (catagen), and a resting phase (telogen). In mice, the developmental phase of HF growth completes around postnatal day 19 followed by the first catagen phase. After follicle regression, the first postnatal hair cycle is initiated at approximately postnatal day 21 and lasts until weeks 6–7. After regression of the HFs, they enter a long telogen phase, extending for at least 3 weeks. Importantly, until this point, the first phase is synchronous across the entire back skin of the animal, whereas subsequent phases of HF growth are asynchronized. Interestingly, the IFE closest to INF is affected by HF growth (Roy et al, 2016); however, it remains unclear whether cell fate decisions in INF are also affected.

Fate mapping data in combination with statistical modeling provide quantitative insights into the cellular dynamics that collectively maintain tissues at the population scale. This type of analysis has been used in many tissues to delineate the behavior of stem cells and progenitors and has been used in the IFE and the SG to describe how these parts of the epidermis are maintained long term in steady state and in cases of insults in the tissue (Andersen et al, 2019; Blanpain and Simons, 2013; Clayton et al, 2007; Dekoninck et al, 2020; Fuchs, 2008; Guiu et al, 2019; Han et al, 2019; Klein and Simons, 2011; Mascré et al, 2012; Moad et al, 2017; Sada et al, 2016; Sánchez-Danés et al, 2016; Snippert et al, 2010; Teixeira et al, 2013). In this study, we extend this type of analysis to INF, where we describe the cellular mechanisms of INF formation and maintenance. Using the *Lrig1::eGFP-IRES-CreER*^{T2} genetic mouse model (Jensen et al, 2009; Snippert et al, 2010), we labeled the cells during early INF formation and adulthood. This approach allowed us to trace the dynamics of labeled progenies during tissue morphogenesis and, when conducted with multiple time points at clonal resolution, the eventual dynamics that support the turnover of adult INF.

RESULTS

Defining cellular growth and behavior during INF morphogenesis

The INF is a stratified epithelium characterized by basal cells anchored to the basement membrane and differentiated suprabasal cell layers (Figure 1a and b) (Fuchs, 2008; Müller-Röver et al, 2001). To understand how INF forms at the cellular level, we first investigated the overall pattern of growth during late development, focusing on small zigzag hairs (Driskell et al, 2009), as described previously for the SG (Andersen et al, 2019). Development of the INF, defined as the structure that spans the upper part of the pilosebaceous from the IFE to the basal cell by the duct of the SG (Figure 1b), is characterized by an initial burst in growth from postnatal day 2 to postnatal day 7, followed by a second slower growth phase that ensures that the INF reaches the size of the adult compartment by postnatal day 23 (comprising 128 ± 12 basal cells) (Figure 1c and Supplementary Figure S1a–d). This is earlier than the structurally similar IFE, where the rapid expansion phase lasts for the first 3 weeks, followed by a slower growth phase before the tissue enters a homeostatic state (Dekoninck et al, 2020).

To define cellular dynamics during morphogenesis in INF, we performed quantitative fate mapping within the upper pilosebaceous unit by labeling progenitors expressing *Lrig1* clonally at postnatal day 2 (Figure 1d–f) (Blanpain and Simons, 2013). Assessment of the 3-dimensional clone composition at postnatal day 7 revealed a broad distribution of basal and suprabasal clone sizes, marked by an exponential-like dependence (Figure 1g and h). Characterized by a single size scale, this behavior suggests that all progenitor cells have the potential to contribute equally to INF morphogenesis. To test this quantitatively, we applied a statistical modeling-based approach to the clonal data (Andersen et al, 2019; Clayton et al, 2007; Mascré et al, 2012), assuming a single population of proliferative basal cells that can divide symmetrically into 2 basal cells (P -> P + P), asymmetrically into basal and suprabasal cells (P -> P + D), or symmetrically into 2 suprabasal cells (P -> D + D). Suprabasal cells do not divide even during the early stages of development. For simplicity, we assumed that the loss of suprabasal cells at early time points was negligible. With 3 fitting parameters (2 for the relative probabilities of fate choices and 1 for the division rate), we found that the distribution of basal and subrabasal cells could be captured accurately over the developmental time course with the probability of symmetrical P + P fate set at 63% (confidence interval = 55–70%), D + D fate at 20% (confidence interval = 0–40%), and the remaining 17% of divisions leading to an asymmetrical fate outcome, P + D. The average division rate of the progenitors was set to once per 1.25 days (Figure 1i and j). The pronounced bias toward symmetric cell duplication fuels the expansion of the compartment, such that each basal cell at postnatal day 2 gives rise to almost 6 cells on average (4 basal, 2 suprabasal) at postnatal day 7, consistent with the nearly 6-fold expansion of the overall tissue (Figure 1c). To further test the predicted average cell cycle time, we measured the cell division rates on the basis of the fluorescence decay of doxycycline-inducible H2B-mCherry (Andersen et al, 2019) (Figure 1k–m). The reduction in the average H2B-mCherry intensity within the basal INF cell compartment followed an exponential-like decay that fit well with the division rate inferred from the clonal data (Figure 1j).

Overall, these data support a model in which the basal layer of the INF is composed of equipotent progenitors that undergo stochastic yet imbalanced cell fate choices to fuel the rapid growth phase.

Long-term cell fate decisions in the adult INF

To understand how INFs were maintained after the initial growth phase, we analyzed samples isolated after the establishment of a homeostatic state (Figure 2a). As expected, the clones were confined within the boundaries of the INF and distributed along the entire compartment axis (Figure 2b). Over time, some clones were found to extend across the length of the INF (Figure 2b). Quantitative clonal analysis revealed a progressive increase in the average number of basal and suprabasal cells in the individual clones (Figure 2c and d). Importantly, the increase in clone size was

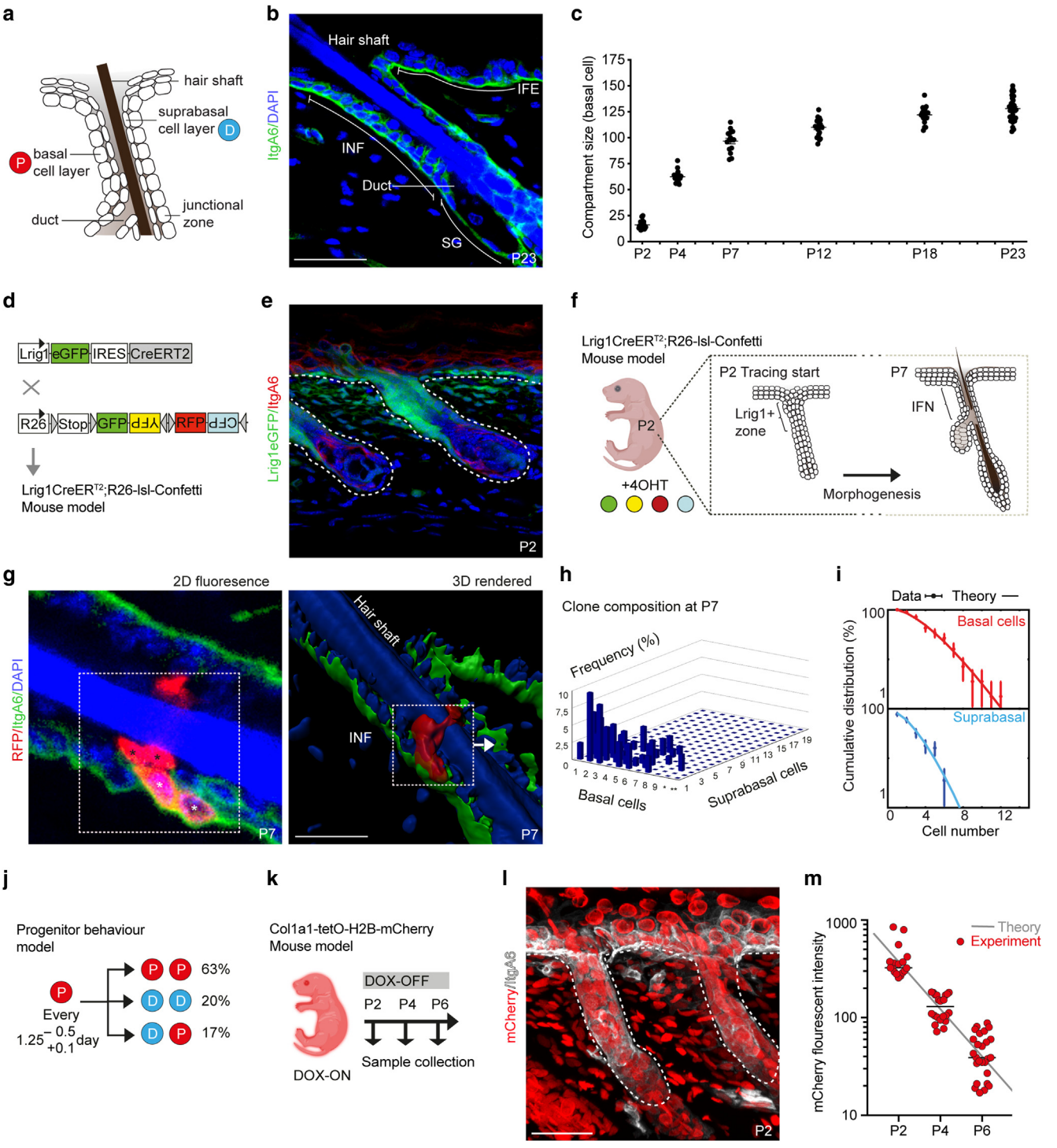

Figure 1. Defining the patterns of tissue growth and cell behavior during INF morphogenesis. (**a**) Schematic depiction of INF structure in adult mice. (**b**) IHC close up of INF stained for DAPI and ITGA6, which marks basal cells. (**c**) Mean number of basal cells in INF at different developmental time points. (**d**) Schematic representation of the mouse model used in the study. (**e**) *Lrig1*eGFP expression at P2 prior to the formation of the INF and at the time of label initiation for this study. (**f**) Illustration of the labeling strategy and the morphological changes in the HF and INF during the course of the lineage-tracing study. Shown are representative 3D reconstruction and 2D images for quantification of an RFP (red) clone at P7. (**g**) ITGA6 staining is used to discern between basal cells (ITGA6+ in green, indicated with white starts) and suprabasal cells (ITGA6−, indicated with black stars). (**h**) Quantification of clone composition (basal and suprabasal cells) and frequency at P7. (**i**) Mathematical analyses based on an effective model with a single stochastic and equipotent progenitor pool, heavily biased toward symmetric renewal, provides the best fit for the experimentally observed clonal data at P7. (**j**) Prediction of probabilities for either symmetrical (producing 2 progenitors or differentiated cells) or asymmetrical (producing 1 progenitor and 1 differentiated cell) cell division every 1.25 days on average from P2 to P7. (**k**) Strategy for independent cell cycle length estimation using the *Col1a1-tetO-H2B-mCherry* mouse model after a 2-week DOX pulse and then chased from P2. (**l**) Representative image of detection of H2B-mCherry (red) and ITGA6 (gray); developing follicles are outlined with a dashed line. (**m**) Intensity of H2B-mCherry fluorescence in the basal compartment of the INF at the indicated time points (experimental data, red circles) has a good fit with the H2B-mCherry fluorescence intensity predicted by the theoretical model in **j** (theoretical model prediction, gray line). Bars = 50 μm. 2D, 2-dimensional; 3D, 3-dimensional; DOX, doxycycline; HF, hair follicle; IHC, immunohistochemistry; INF, infundibulum; P2, postnatal day 2; P7, postnatal day 7.

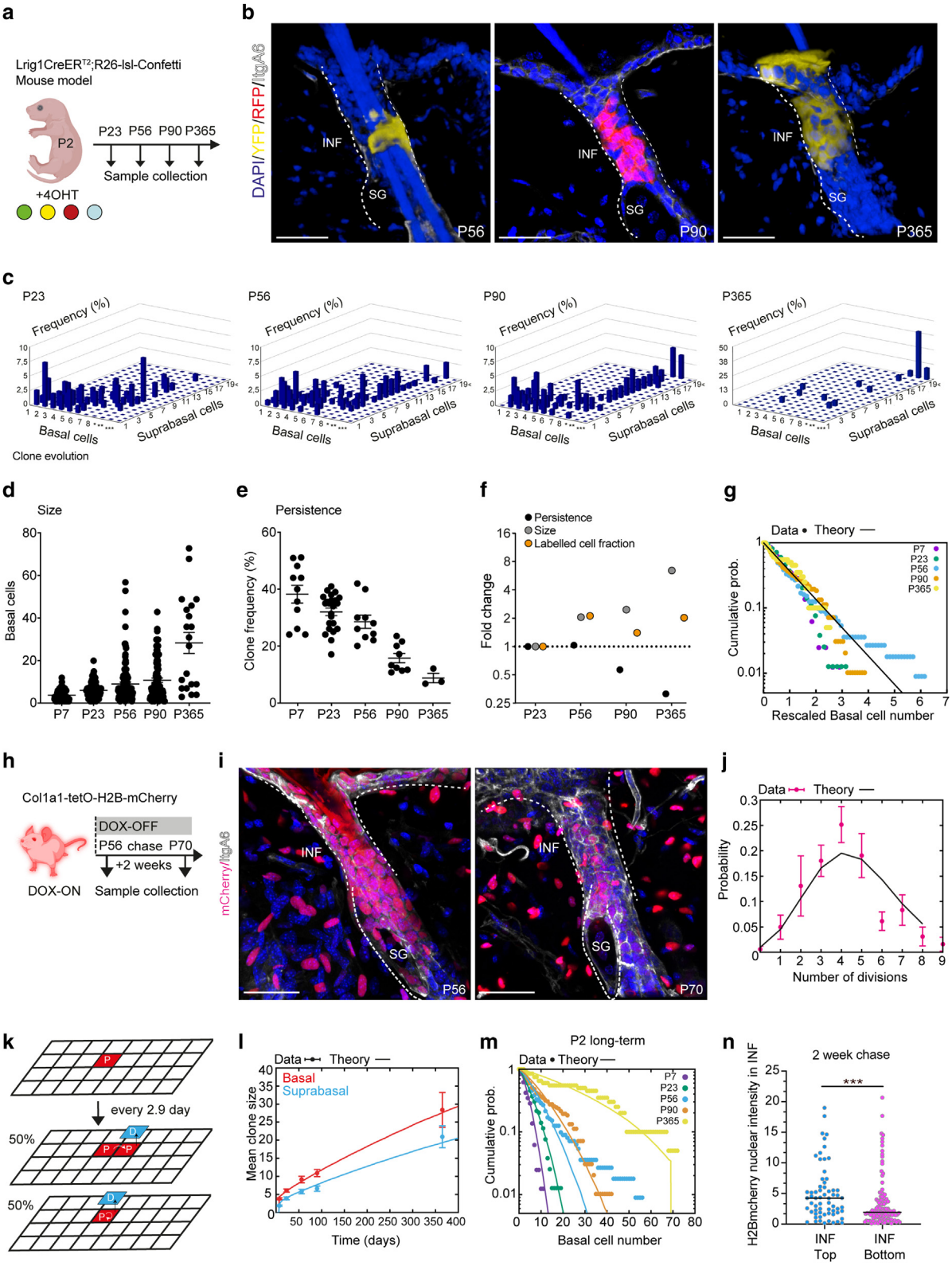

Figure 2. Long-term cell fate decisions in the adult INF follow neutral drift dynamics. (**a**) Schematic representation of tissue collection at different timepoints in adult homeostasis. (**b**) Representative images of RFP and YFP clone detection in the INF (follicle outlined with dotted lines) at different time points in rendered confocal z-stacks, basal cells (ITG6A+) in gray. (**c**) Quantification of clone composition (number of basal and suprabasal cells per clone) and frequency at different developmental time points. (**d**) Number of basal cells per clone at different developmental time points. (**e**) Persistence of clones over time. Labeled cell fraction, clone size, and persistence at different developmental time points are shown. (**f**) Dotted line indicates the predicted labeled cell fraction in the case of neutral drift dynamics based on an equipotent progenitor model at the indicated time points relative to P23. (**g**) Experimental basal clone size distributions (dots, same as dataset in **c**–**e**) versus theoretical distribution generated in a biophysical analysis based on an effective model with a single equipotent progenitor pool at all time points. (**h**) Strategy for cell cycle analyses using *Col1a1-tetO-H2B-mCherry* mouse model. (**i**) Representative images used for H2B-mCherry detection

accompanied by a decrease in the number of clones detected per INF (defined as clone persistence) (Figure 2e). This suggests that, similar to IFE and SG (Andersen et al, 2019; Dekoninck et al, 2020; Mascré et al, 2012), cells in the basal layer continuously compete with their neighbors. Notably, the labeled cell fraction, that is, the number of label cells per unit area (number of clones × size of clones), remained largely constant over the course of the study, indicating that the clonally labeled population was representative of the tissue (Figure 2f). Importantly, at all time points in adult INF, the clones collapsed well onto an exponential-like size distribution (Figure 2g), demonstrating that the *Lrig1* promoter marks a population of INF cells that compete neutrally for long-term and compartment-wide INF maintenance. Only a small fraction of the clones (<5%) occupied the majority of INF, even at the longest time point (postnatal day 365) (Figure 2d and g).

Before attempting to model the pattern of cell fate decisions in homeostasis, we wished to limit the number of free parameters by independently measuring the basal cell division rate during homeostasis once again on the basis of the fluorescence decay of doxycycline-inducible H2B-mCherry. The decay in H2B-mCherry expression showed that the cells divided on average once every 2.9 days (Figure 2h–j). Next, we tested whether the most parsimonious model, involving equipotent progenitors choosing stochastically between symmetric cell division (expelling one of their nearest neighbors to the differentiated suprabasal layer) and intrinsically asymmetric division (leading to 1 basal cell and 1 suprabasal cell) with nearly equal probability (Figure 2k), could explain both clonal and H2B-mCherry dilution datasets with the same division rate. We found that the model provided a good quantitative prediction of the distribution of the number of cell divisions over the 2-week chase period in the H2B-mCherry model (H2B-mCherry dilution) (Figure 2k) as well as for the temporal evolution of mean basal and suprabasal clone sizes and clone size distributions (Figure 2l and m and Supplementary Figure S2a–d and a′–d′).

In conclusion, these results suggest that the maintenance of INF parallels that of IFE and SG, with a single population of equipotent basal progenitors that maintain tissue through a process of stochastic fate choices (Andersen et al, 2019; Dekoninck et al, 2020; Mascré et al, 2012).

Niche-specific stem cell behaviors in the adult INF (top vs bottom)

Despite the success of the model in recapitulating clone dynamics, we considered whether the innate temporal and morphological heterogeneity of INF could impact finer scales. In particular, INF is subject to potential influences from hair growth and the follicular cycle (Müller-Röver et al, 2001). Indeed, when looking closely at our H2B-mCherry pulse/chase experiments, we found that after a 2-week chase, basal progenitors located at the bottom of the INF displayed significantly lower nuclear fluorescence intensity of H2B-mCherry than their counterparts in the upper INF (Figure 2n). Importantly, although we started the chase at postnatal day 56, when the follicle was in telogen, during the course of the 2-week chase period, the follicles progressed to anagen. These results imply that cells at the bottom of the INF undergo more rounds of cell division, thereby diluting the H2B-mCherry signal faster than progenitors located at the top of the INF.

At first sight, such behavior is at odds with our minimal modeling analysis that suggested that all cells along the INF axis behaved in a similar manner. To further address whether the hair cycle affects cell behavior within the INF and challenge our assumption of equipotent progenitors along its length, we performed 5-ethynyl-2′-deoxyuridine (EdU) pulse-chase experiments, labeling replicating cells in adult mice that displayed synchronous and asynchronous hair growth in the anagen and telogen follicles (Figure 3a). This analysis allowed us to identify the differences in the number of replicating cells between those located at the top and bottom of the INF. In the anagen phase, we observed an approximately 2-fold increase in the number of EdU-positive cells in the INF compared with that in the telogen phase (Figure 3b–d and Supplementary Figure S3a and b). Moreover, although replicating cells were distributed evenly throughout the INF in the telogen phase, we observed that the increase in EdU-positive cells during the anagen phase was predominantly located in the lower half of the INF (Figure 3d). The increase in replicating cells was mirrored by a transient increase in the size of INF during the anagen phase (Figure 3e and Supplementary Figure S3c and d). In addition, there was a transient increase in basal cell number and density when comparing the total number of ITGA6+ basal cells at the top and bottom of the INF, specifically during the short window of time that the HF was in the anagen phase (Figure 3f–i). In this study, the increased size of the INF led to a lower cell density in the upper part of the INF, owing to a constant number of basal cells (Figure 3h and i). In line with these observations, we found that although clones induced at postnatal day 7 were largely isotropic 5 days after labeling, they became anisotropic as they underwent multiple cycles of HF growth (Supplementary Figure S3f and g). The relationship between short-time-scale dynamics and compartment size, cellular density, and spatial changes in the fraction of proliferating cells indicated that INF maintenance was governed by previously unappreciated, flexible, and

for cell cycle analyses. (**j**–**m**) Experimentally determined distribution of cell divisions within a 2-week period (dots with SEM) compared with a theoretical model best fitted cell cycle time of 2.9 days (black line). (**k**) Schematic representation and (**j, l, m**) predictions of our biophysical modeling of INF homeostatic turnover. Basal cells are simulated on a 13 × 10 cylindrical grid and can either symmetrically divide (expelling one of their nearest neighbors to the suprabasal layer) or asymmetrically divide into 1 basal and 1 suprabasal cell. (**j**) The H2B-mCherry dilution data, (**l**) temporal evolution of mean clone size (basal in red, suprabasal in blue), and (**m**) basal clone size distribution from P7 to P365 can be fitted well by a model of equipotent stochastic progenitors dividing on average every 2.9 days and with near equal probability of symmetric and asymmetric divisions (Materials and Methods provides the details). Lines represent the prediction from the theoretical model, whereas dots represent (**j**) experimental data obtained from H2B-mCherry nuclear fluorescence intensity and (**l, m**) clone analyses and quantification at different time points. H2B-mCherry nuclear fluorescence intensity in cells of the INF in different locations along the compartment axis. (**n**) Cells in the INF located closer to the IFE are referred to as top cells, cells located at the base of the INF closer to the SG and -isthmus are referred to as bottom cells. Bars = 50 μm. IFE, interfollicular epidermis; INF, infundibulum; P23, postnatal day 23; P7, postnatal day 7; P365, postnatal day 365; SG, sebaceous gland.

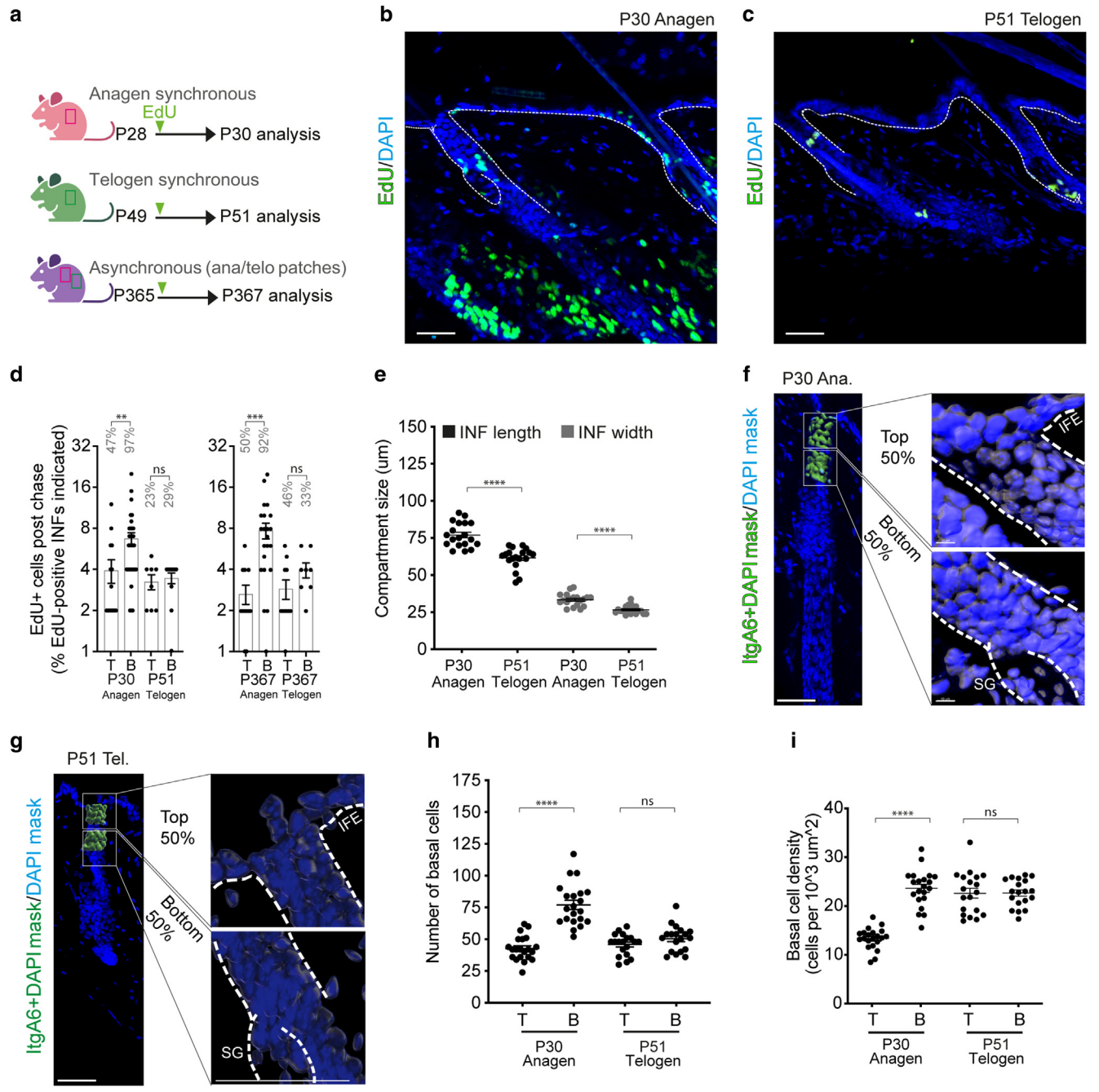

Figure 3. Transient spatiotemporal cellular dynamics in the INF anagen growth and telogen rest phases. (**a**) Schematic representation of experiments designed to label replicating cells to determine replication rate in anagen vs telogen follicles. Representative confocal images of follicles (outlined with dotted white line) used for EdU (green) detection in (**b**) anagen and (**c**) telogen. (**d**) Quantification of EdU-positive cells along the length of the INF at different time points during anagen and telogen. (**e**) Quantification of length and width of the INF in anagen and telogen follicles. (**f, g**) Representative 3D reconstruction rendered confocal images of basal cells (ITGA6+) in the top and bottom parts of the INF in anagen and telogen. (**h**) Quantification of number of basal cells in top and bottom of INF in anagen and telogen. (**i**) Quantification of basal cell density of images shown in **f** and **g**. Bars = 50 μm and 10 μm for the insert in **f**. 3D, 3-dimensional; EdU, 5-ethynyl-2′-deoxyuridine; INF, infundibulum; ns, not significant.

location-specific cellular behaviors that were influenced by the transition between anagen- and telogen-specific states.

Next, we investigated how to integrate these findings with our lineage-tracing experiments, suggesting global equipotency. To assess whether cell behavior in the homeostatic epithelium (after postnatal day 21) is characterized by an equal contribution from cells at the top and bottom of the INF, we took advantage of the restriction of *Lrig1* expression to the bottom of the INF in fully formed HFs (Supplementary Figure S4a). Specifically, to trace the contribution of cells in this region to the long-term maintenance of tissues, we performed high-density labeling using the *Lrig1::eGFP-IRES-CreER^{T2}; Rosa-lsl-Confetti* mouse model (Figure 4a–e and Supplementary Figure S4b–e). On the basis of our statistical model of cell fate decisions from homeostasis (Figure 2k), we could predict with high accuracy the volume and persistence

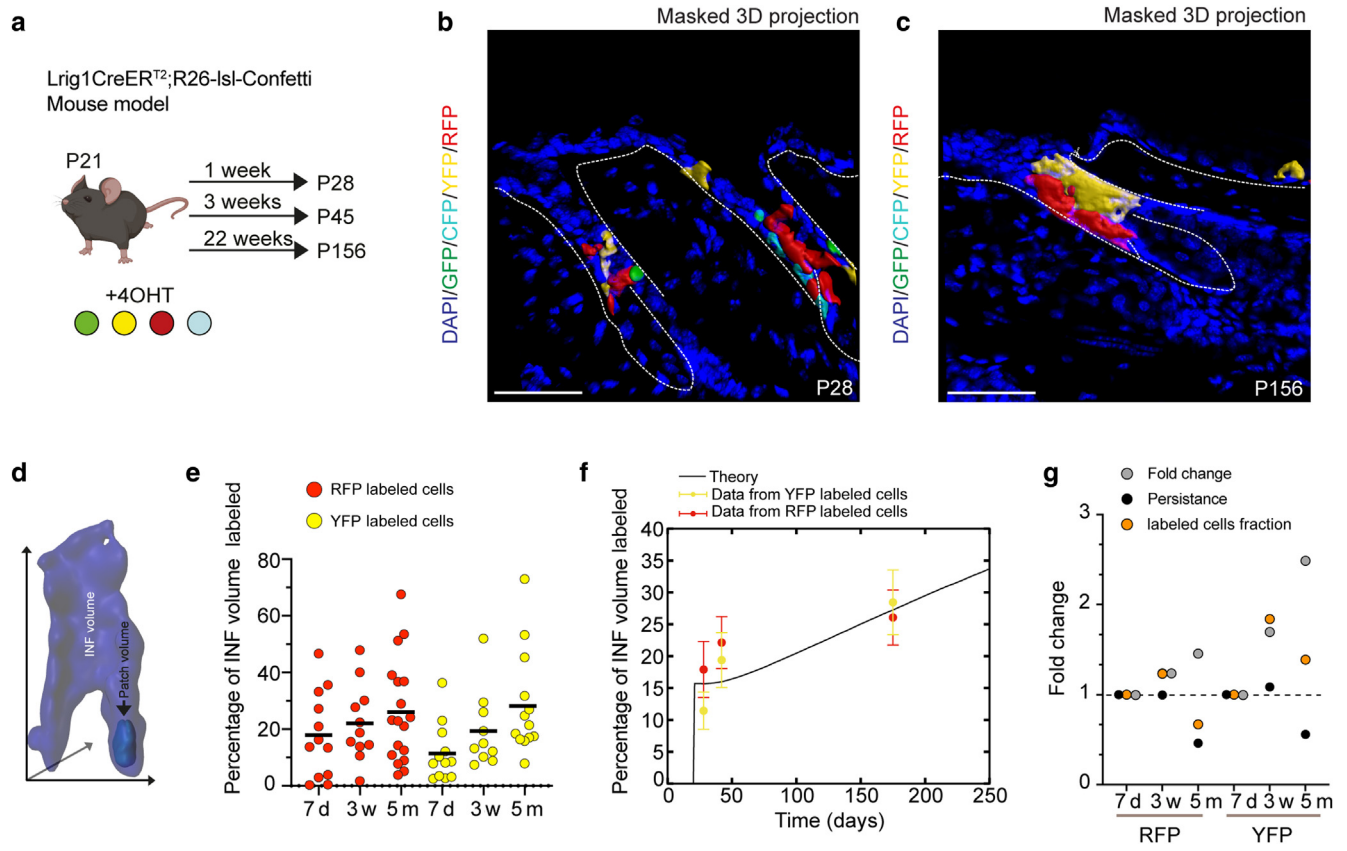

Figure 4. In the long term, cells located at the bottom of the INF do not outcompete their counterparts at the top of the INF. (**a**) Schematic representation of high-density labeling of the "bottom" population of cells in the INF. (**b, c**) Representative 3D reconstructions of resulting "patches" of labeled cells at P28 and P156. (**d**) Schematic representation of clone volume quantification versus total infundibulum volume. (**e**) The results of the analyses. (**f**) Predictions from our theoretical model described in Figure 2, changing only the initial condition for labeling at P21, provides a good prediction of labeled cell "patch" volume in the INF (black line); experimental data for RFP and YFP INF-labeled cell volume are displayed as red and yellow dots. Shown are labeled cell fraction, clone size, and persistence at different time points after labeling initiation for RFP and YFP clones. (**g**) Dotted line indicates the predicted constant labeled cell fraction for representative labeling of a progenitor population, at the indicated time points relative to those 7 days after labeling. Bars = 50 μm. 3D, 3-dimensional; INF, infundibulum; P156, postnatal day 156; P21, postnatal day 21; P28, postnatal day 28.

of the resulting "patches" of labeled cells (Figure 4g and Supplementary Figure S4f). Interestingly, we found that the fraction of labeled cells remained constant over a 5-month time course (Figure 4g). This indicated that although cells at the bottom of the INF showed a transient phase of elevated proliferation during anagen, this did not lead to an accelerated and preferential replacement of cells at the top of the INF during the tracing period. Moreover, this conclusion was reinforced by the analysis of an extended model that considered proliferation gradients along the top–bottom axis of the INF. These results showed that the overall predictions of the clonal dynamics over the long term were only mildly altered by transient changes in proliferation, a result that could be rationalized on the basis of the local nature of competition between basal cells and their nearest neighbors (Materials and Methods and Supplementary Figure S4g and h provide the details).

Spatiotemporal tissue dynamics define the adult INF (anagen vs telogen)

To further elucidate the impact of HF growth induction on cellular behavior within the INF, we stimulated the transition from HF to anagen using local depilation. We then initiated clonal labeling and assessed clonal growth (Figure 5a–e). Importantly, depilation-induced anagen recapitulated the same changes in the size and basal cell density of INF as those observed in the natural anagen phase. This was evident as early as 2 days after depilation (Figure 5d–g and Supplementary Figure S5a–j). Importantly, nondepilated areas remained in the telogen stage (Figure 5f and g and Supplementary Figure S5d and f). Furthermore, analysis of the clonal data revealed an increase in the basal cell fraction of clones in induced anagen follicles, especially those located at the bottom of the INF (Figure 5h–j), whereas the suprabasal fraction remained unchanged between telogen and anagen follicles (Figure 5k). This suggests that the anagen phase is not only characterized by a transient increase in the number of proliferating cells, as evidenced by our EdU experiments, but also by a transient shift in cell fate toward the production of basal cells. This was supported by statistical modeling of the lineage-tracing dataset, which showed a 15% increase in the probability of producing progenitor/basal cells from cells located at the bottom of the INF compared with that from nonwaxed telogen controls (Supplementary Figure S5k and l).

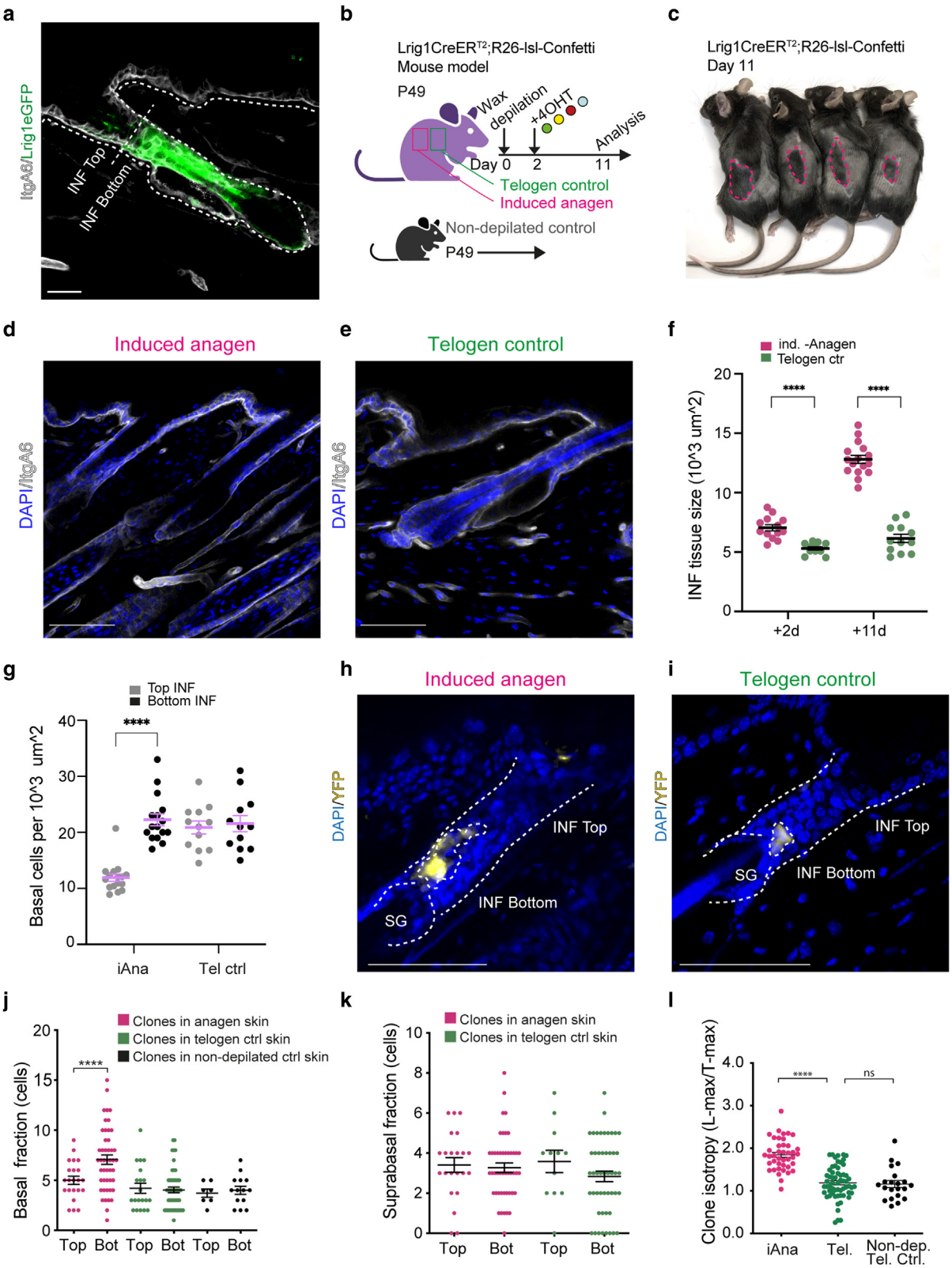

Figure 5. Anagen promotes a transient cell fate shift in the bottom of the INF. (**a**) *Lrig1*-eGFP expression in a telogen follicle of a P49 mouse, ITGA6 (gray), and *Lrig1*eGFP expression in green. (**b**) Outline of strategy for labeling of cells and anagen induction. Shown is photo of shaved mice 11 days after waxing. (**c**) Waxed areas are darker owing to the activity of melanocytes during anagen, whereas surrounding nonwaxed areas remain in telogen and are lighter in color; depilated areas are outlined with magenta dotted line. (**d**) Representative confocal image of follicles in waxed areas appear to be in anagen, (**e**) whereas nonwaxed areas remain in telogen. (**f, g**) Quantification of INF tissue size and basal cell density respectfully in anagen versus telogen HF. (**h, i**) Representative confocal images of clones in induced anagen or telogen follicles. (**j, k**) Quantification of basal and suprabasal cell number, respectively, in clones at the top or bottom of INF in induced anagen or telogen follicles. (**l**) Isotropy measurement of clones in INF from iAnagen and telogen follicles in waxed mice as well as measurements from an unwaxed control mouse in telogen. Bars = 100 μm. INF, infundibulum; P49, postnatal day 49.

This temporary imbalance between the behavior of the cells at the top and bottom of the INF was further reflected in the isotropy of the clones. In telogen follicles, clones were isotropic, whereas in anagen follicles, clones were anisotropic, displaying a preference for growth directionality (Figure 5l and Supplementary Figure S5m). Collectively, these data demonstrate the dynamic cellular behavior within the INF as it passes through its natural cycles of growth and rest.

DISCUSSION

In this study, we showed that INF are formed by a pool of equipotent basal progenitors that undergo a temporally conserved pattern of stochastic cell fate. By postnatal day 23, when the INF reaches its full size, it switches to a homeostatic replenishment program, where local cell competition between neighboring basal progenitors results in a pattern of balanced stochastic fate within the confines of the INF niche. Surprisingly, we found that INF underwent substantial and transient remodeling during each cycle of hair growth. Investigating this further, we found that even though basal progenitors in the INF show long-term equipotency, the basal cells at the bottom of the INF display a transient increase in proliferative activity and a temporal fate shift that allows them to produce more basal cells than their counterparts at the top of the INF. However, when the follicle returned to telogen, no difference was observed in the number of proliferative cells or the proportion of basal cells produced, on average, between progenitors at the top and those at the bottom of the INF. Thus, the proliferative advantage of the cells at the bottom of the INF layer was transient. This illustrates that even though a tissue can be represented by an equipotent progenitor model over extended periods of time, where cells undergo stochastic loss and replacement, they can exhibit a temporal imbalance in cell fate choices if this advantage is followed by compensatory cell loss. Interestingly, cells of the IFE surrounding HFs have been shown to exhibit similar behavior during active hair cycling (Roy et al, 2016).

Notably, we assessed INF cellular dynamics through an *Lrig1CreER* clonal assay, but we systematically observed that the clones were representative of the behavior of the overall tissue. This was exemplified by a nearly 6-fold expansion between postnatal day 2 and postnatal day 7 (Figure 1c), followed by a nearly constant labeled cell fraction both after postnatal day 7 in the postnatal day 2 tracing and the postnatal day 21 tracing, as expected during homeostasis. Thus, although we cannot exclude the possibility that this quantitative lineage-tracing assay misses small subpopulations of stem cells and/or committed progenitors, the close match between clonal and tissue behavior suggests that the putative contributions from other cellular populations would need to be small (Mascré et al, 2012; Sánchez-Danés et al, 2016). Similarly, we only modeled proliferative basal and non-proliferative suprabasal cells, assuming instantaneous transfer between the different layers upon differentiation. Although intermediary steps and/or cellular states could be added in this model, such as transitional cells in the basal layer (Cockburn et al, 2022; Wang et al, 2020), this would not change the long-term dynamics of the size distribution that we studied.

Prior qualitative studies have revealed that *Lrig1*-expressing cells located within the junctional zone support INF maintenance (Andersen et al, 2019; Page et al, 2013; Veniaminova et al, 2013). Notably, in qualitative fate-mapping studies, it is only possible to draw conclusions on the behavior of labeled cells. The quantitative analysis performed in this study clearly demonstrates that cells irrespective of their location in the INF have the capacity to contribute long term to its maintenance. Thus, *Lrig1*-expressing cells located in the junctional zone, although show transient changes in their proliferative features during the hair cycle, are no longer likely to contribute to INF maintenance compared with cells located at the top of the INF. It will be interesting to address whether cells in the upper INF upon injury would be similar to *Lrig1*-expressing cells in the junctional zone and display a greater contribution to tissue regeneration (Aragona et al, 2017).

With the establishment of cell behavior in the INF, all major parts of the epidermis (IFE, SG, INF, and HF proper) have been traced using quantitative fate mapping in combination with mathematical modeling (Andersen et al, 2019; Clayton et al, 2007; Dekoninck et al, 2020; Roy et al, 2016; Mascré et al, 2012; Sada et al, 2016). Similar to other organs, the major mode of cell replenishment across all tissue components in the epidermis can be explained within the framework of an equipotent progenitor model, with quiescent stem cells playing only a minor role in the day-to-day maintenance of tissues, at least in mice (Andersen et al, 2019; Dekoninck et al, 2020; Klein and Simons, 2011; Piedrafita et al, 2020). Interestingly, temporal activation of stem cells in the HF bulge leads to their involvement in every hair cycle. However, it does remain unclear how the growth of the HFs can influence the remaining part of the epidermis. Such effects could involve changes in the biophysical properties of the tissue and the availability of GFs/cytokines. Our study revealed a previously unappreciated and finely tuned regulation of the INF niche as the HF goes through its natural cycle of growth and rest. It will be interesting to study in the future what local signals in the microenviroment facilitate these temporary transitions and how they are regulated.

MATERIALS AND METHODS

Mice

This study utilized the mouse models *Lrig1::eGFPiresCreER^{T2}* (Page et al, 2013) and *Rosa26-lsl-Confetti* (Snippert et al, 2010). *R26-TTA/TTA:Col1a1-tetO-H2B-mCherry* mice were purchased from JAX (stock number 014602) (Beard et al, 2006). The C57BL/6J mice used for the EdU pulse-chase experiments were purchased from Taconic. Mouse colonies were housed in specific pathogen-free animal facilities with a 12-hour light–dark cycle and ad libitum access to food and water. The Animal Experiments Inspectorate of Denmark reviewed and approved all animal procedures (permit numbers 2017-15-0201-01381 and 2023-15-0201-01378). Female and male mice were used for all experiments with an equal animal sex ratio in the majority of the analysis.

Lineage-tracing experiments

For clonal induction, *Lrig1CreER^{T2}-R26Confetti* mice were treated topically with a single application 100 μl of 4-hydroxy tamoxifen dissolved in acetone (99%, Sigma-Aldrich). The solution was spread

evenly on an approximately 2-cm^2 area of the back skin closest to the tail of the mice at postnatal day 2. When applied to the adult mice, the area was first shaved before the solution was used. For the high-dose experiments in adults, a single dose of IP 4OHT-tamoxifen dissolved in 100% ethanol and resuspended in an oil solution with addition of PBS was administered.

Cell proliferation

To measure the number of replicating cells at given time point, we administered an intraperitoneal injection of EdU (Thermo Fisher scientific), 8.3 μg/gram of weight of the mouse, dissolved in saline. EdU was then detected using the Click-IT Alexa-Fluor 647 Imaging Kit (Thermo Fisher Scientific) in thick frozen sections that received an hour-long paraformaldehyde fixation prior to freezing on optimum cutting temperature. To measure the cell proliferation kinetics, we used H2B-mCherry mice. To induce maximum labeling, the mice were kept on 2 g/kg doxycycline food pellets (Ssniff-Spezialdiaten GmbH) for 2 weeks prior to the initiation of the experiment.

Immunohistochemistry

For frozen sections, the back skin collected from mice was fixed in 4% paraformaldehyde for an hour at room temperature and then embedded in the optimum cutting temperature compound (Cell Path). Paraffin-embedded back skin tissue was fixed in paraformaldehyde at 4 °C overnight before transferring the tissue in 70% ethanol for further processing and embedding in wax. For analyses of basal/suprabasal composition of clones, tissue frozen in optimum cutting temperature was cut on a cryostat into 70−90 μm sections (Leica Microsystems CM3050S). These sections were then incubated for 1 hour in 0.5% BSA, 0.5% fish skin gelatin, and 0.1% Triton X/100 in PBS and then incubated overnight in the same solution with the relevant antibodies. Sections were washed at minimum of 3 times in PBS containing 0.05% Triton x-100 before another overnight incubation with the relevant secondary antibodies and DAPI. The sections were then washed again and spread onto slides for imaging in a Mowiol solution.

Paraffin embedded section (3−4 μm) were stained after rehydration and antigen retrieval in citric acid (pH 6.0) under pressure. Sections were blocked for an hour in blocking buffer, followed by incubation for 1 hour at room temperature or overnight at 4 °C with primary antibodies. The sections were then washed with 0.05% Triton x-100 in PBS at 3 × 10 minutes and incubated with secondary antibodies for 45−60 minutes using DAPI. Finally, the sections were washed and mounted with Mowiol.

Three-dimensional imaging was performed using a laser-scanning confocal microscope (Leica TSC SP8). Images were analyzed after the 3-dimensional reconstruction of z-stacks using IMARIS and Fiji software.

Statistics and reproducibility

The number of biological and technical replicates is indicated in the figure legends and main text. Details on the biophysical modeling of INF and the statistical tests used to study the cellular dynamics of INF at different stages of development and growth are provided earlier.

The sample size was not predetermined in this study. No randomization or blinding was performed to analyze the experimental data. For all the experiments, the error bars represent the SEM or SD. Mann−Whitney nonparametric tests were used to assess the significance of the variations in the datasets.

Theoretical note

To analyze the patterns of cell fate decision making during neonatal growth and homeostasis, we sought to define the simplest model that was compatible with the results of lineage tracing and morphometric analysis data. On the basis of the stratified architecture of the INF, we chose, as a minimal model, one in which the basal cell layer comprises a single equipotent pool of progenitors P, which divide and differentiate, giving rise to nonproliferative suprabasal cells, D. With a constant division at rate λ_P, we considered 3 possible fate outcomes:

$$P \rightarrow \begin{cases} P + P \text{ at rate } r + \Delta \\ P + D \text{ at rate } 1 - 2r \\ D + D \text{ at rate } r - \Delta \end{cases}$$

where the parameter r fixes the relative frequency of symmetric to asymmetric fate, and the parameter Δ determines the degree of cell fate bias toward symmetric duplication. At homeostasis, the degree of imbalance $\Delta = 0$ (to ensure that the number of basal progenitors remains constant over time), whereas suprabasal cellular loss at some constant rate ensures that the number of suprabasal cells remains in steady state. In the context of development, the degree of imbalance Δ must become nonzero to ensure that basal cells expand in proportion to the area of the INF. Further details on the clonal dynamics of this model can be found in previous studies (Andersen et al, 2019; Dekoninck et al, 2020). However, a key prediction of the stochastic model above is that within this framework, the basal clone size distributions are predicted to converge toward a universal exponential scaling form $P(k) = \frac{e^{-k/<k>}}{<k>}$, where $< k >$ denotes the average clone size at a given time point. At homeostasis, this average is predicted to grow linearly over time at rate $r\lambda_p$, translating to the effective rate of stem cell loss/replacement (Klein and Simons, 2011). Notably, the stochastic cell fate model described our clonal dataset well (Figure 2g) at all time points, providing the first qualitative test of the theory. Another important qualitative control was to check whether the labeled cell fraction at homeostasis (defined by the product of clonal persistence and average surviving clone size) was constant over time (Figure 2f). This suggests that the population traced by Lrig1CreER is homeostatic and thus representative of the overall tissue.

Quantitatively, before turning to homeostasis, we first examined the postnatal day 2 lineage-tracing dataset to understand infundibular growth. Given that we are examining a rather small-time window (postnatal day 2 to postnatal day 7), we reasoned that we could strongly constrain the different parameters (r, Δ, λ_p) on the basis of the joint fitting of the basal and suprabasal clone size distribution at postnatal day 7 and use the H2B-mCherry dilution experiments as a test of the fit. We followed an approach similar to that of Andersen et al (2019), to which we refer for further details. In short, we used a method of least-squares fitting on the distributions $P(n_P)$ and $P(n_D)$ for the basal and suprabasal clone sizes, respectively, and minimized the residuals with respect to (r, Δ, λ_p). We identified the best-fit parameter set, which was unique (fitting both distributions well, as depicted in Figure 1i) and used a bootstrapping method (Monte Carlo algorithm for case resampling) to estimate the confidence intervals of these parameters in a nonparametric manner. We reported the 95% confidence intervals in the main text and figures. These results were consistent with a strong bias toward symmetric cell duplication, with a division rate of approximately once per day (Figure 1j). This estimate was consistent with the results of the H2B-

mCherry dilution assay (Figure 1m). Moreover, this rapid rate of cell division, with nearly 60% of divisions resulting in a symmetric fate outcome, was also consistent with the rapid 6-fold increase in overall compartment size observed between postnatal day 2 and postnatal day 7 (Figure 1c), suggesting that the dynamics of the LRIG1 population, which we traced at postnatal day 2, are representative of the morphogenesis of the tissue as a whole. We followed a similar procedure to fit the short-term postnatal day 49 + 9-day datasets in unwaxed and waxed samples, which was consistent with an enhanced imbalance toward symmetric renewal in waxed samples (Supplementary Figure S4k and l provides the details).

To quantitatively investigate the long-term tracing datasets (postnatal days 2−365), we used a spatial implementation of the model described earlier, in which stochastic cell duplication is precisely compensated for by the differentiation and stratification of a neighbor into the suprabasal cell layer. Such refinement was necessary as the maximal clone sizes at postnatal day 365 approached the overall size of the INF (Figures 1c and 2c), at which point the statistical scaling behavior of clone sizes was predicted to break down, and the 2-dimensional spatial structure of the basal layer created a small logarithmic correction for the average clone size dependence (Klein and Simons, 2011), which can be relevant for long-term tracking. To develop this program, the INF was defined as a 2-dimensional cylindrical grid of 10 × 13 basal cells at postnatal day 7.

To seed the initial distribution of clones on the grid at postnatal day 7, we first numerically simulated the nonspatial model between postnatal day 2 and postnatal day 7 and mapped the resulting stochastic clone sizes onto the grid. We also smoothly interpolated between the division rate λ_p fitted from postnatal day 2 to postnatal day 7 to the homeostatic division rate λ_p^0 that was fitted independently, as defined below, taking a timescale of 2 weeks for neonatal growth (Andersen et al, 2019). From postnatal day 21 onward (after which the overall INF size remained constant), each basal cell division (at rate λ_p^0) results either in a symmetric division, that is, the replacement of 1 of the 4 neighbors $P \rightarrow P + P$ at rate $r\lambda_p^0$ (note that in the top-most and bottom-most row, cells have only 3 neighbors), or in a intrinsically asymmetric division, that is, a suprabasal cell is produced without changing the basal grid configuration, $P \rightarrow P + D$ at rate $(1 - r)\lambda_p^0$. Note that in this incarnation of the model, symmetric differentiation $P \rightarrow D + D$ occurs implicitly when both daughters are expelled by one of their neighbors. It should be noted that asymmetric divisions can occur even when $r = 1$.

To quantitatively compare the full experimental H2B-mCherry distribution with the model, we simulated the H2B-mCherry assay by counting the number of divisions of each basal cell from postnatal day 63 to postnatal day 77 and plotted the resulting distributions over 10^6 repeats of the simulations (Supplementary Figure S2). We started by asking whether we could capture the data without invoking the existence of intrinsically asymmetric divisions ($r = 1$), in which case the only free parameter would be the cell division rate λ_p^0. Although we could fit the data well, this predicted a value of λ_p^0 around 1 division every 6 days, inconsistent with the results of the H2B data at postnatal day 56 (Figure 2h−j), which suggested that most cells had divided 4 times over the course of 2 weeks. However, by increasing the rate of intrinsically asymmetric divisions, we could find the rate at which both datasets were fit: the increase in average clone size is only sensitive to the rate of symmetric divisions $r\lambda_p^0$, whereas the H2B-mCherry dataset is sensitive to the division rate λ_p^0. Thus, by decreasing r, we could find larger best-fit values of λ_p^0, which could also fit the H2B-mCherry dataset. Conversely, if r was too small, we then had to have extremely fast division rates λ_p^0, which overestimated the number of divisions in the H2B-mCherry dataset (Supplementary Figure S2c provide details for sensitivity analysis). More quantitatively, we performed, as described earlier, a bootstrapping method to estimate best-fit values and confidence intervals, by jointly fitting the average basal clone size in time and H2B-mCherry datasets (taking into account the variance in each time point/ probability of each number of divisions). To adequately weigh both datasets (which have very different units: one in terms of basal cell number and the other in terms of density distribution), we weighted all quantities by their experimental average when calculating the total residuals between the model and data. We found that with $r = 0.42$ (confidence interval = 0.2−0.65) and $\lambda_p^0 = 0.22d^{-1}$ (confidence interval = 0.2−0.25 d^{-1}) (ie, 1 division every 3 days), we could obtain a good joint fit of the dataset (Figure 2k−m and Supplementary Figure S2c).

Importantly, because we found experimental evidence for differences in the proliferation rate between top and bottom cells in the INF, we also checked the sensitivity of our results to the introduction of spatial gradients of λ_p^0 in the simulations. Importantly, even strong gradients (50% differences between top and bottom proliferation) did not yield significantly different predictions (Supplementary Figure S4g and h), which is due to the fact that cells only compete with their immediate neighbors (with similar proliferation rates).

With this fully parameterized model, we could also make predictions on tracings from different time points, such as postnatal day 21 induction (Figure 4). In this case, we ran the same simulations but for the initial conditions, which were taken to mimic the initial labeled cell fraction of 15% (Figure 4f). Given the nonclonal nature of the assay, we emphasized the percentage of INF labeled by either RFP or YFP clones, which increased in time owing to neutral drift in a similar manner in both the model and experiments (Figure 4d−f). We also report the persistence of tracing (ie, whether a given INF has labeled cells of a given color) (Supplementary Figure S4). Notably, this experiment also showed that the labeled fraction was still roughly constant within the 5-month tracing period (Figure 4g), which is important as it argues in favor of the equipotency of progenitors and that LRIG1 labels the INF in a representative manner at homeostasis.

DATA AVAILABILITY STATEMENT

No large datasets were generated as a result of this study. The data that support the findings of this study are available from the corresponding author kim.jensen@sund.ku.dk upon request.

ORCIDs

Marianne S. Andersen: http://orcid.org/0000-0001-6751-5453
Svetlana Ulyanchenko: http://orcid.org/0000-0003-3124-9178
Pawel J. Schweiger: http://orcid.org/0000-0001-7659-7462
Edouard Hannezo: http://orcid.org/0000-0001-6005-1561
Benjamin D. Simons: http://orcid.org/0000-0002-3875-7071
Kim B. Jensen: http://orcid.org/0000-0001-6569-1664

CONFLICT OF INTEREST

The authors state no conflict of interest.

ACKNOWLEDGMENTS

We thank the members of the Jensen Laboratory for experimental and technical advice, the imaging facilities at reNEW, and animal caretakers for expert assistance. This work was supported by the Lundbeck Foundation (R105-A9755 to KBJ) and the Leo Pharma Foundation (LF-OC-20-000169). The Novo Nordisk Foundation Center for Stem Cell Medicine was supported by a

Novo Nordisk Foundation grant (NNF21CC0073729). B.D.S. was supported by the Wellcome Trust (219478/Z/19/Z) and a Royal Society EP Abraham Research Professorship (RP/R1/180165 and RP\R\231004). Figure elements were adapted from Bio-Render. KBJ is the lead contact and guarantor of this study.

AUTHOR CONTRIBUTIONS

Conceptualization: MSA, SU, EH, BDS, KBJ; Formal Analysis: EH, BDS; Funding Acquisition: BDS, KBJ; Investigation: MSA, SU, PJS; Supervision: EH, BDS, KBJ; Validation: SU; Visualization: MSA, SU, EH; Writing - Original Draft Preparation: SU, EH, BDS, KBJ; Writing - Review and Editing: EH, BDS, KBJ

SUPPLEMENTARY MATERIAL

Supplementary material is linked to the online version of the paper at www.jidonline.org, and at https://doi.org/10.1016/j.jid.2025.01.034.

REFERENCES

Andersen MS, Hannezo E, Ulyanchenko S, Estrach S, Antoku Y, Pisano S, et al. Tracing the cellular dynamics of sebaceous gland development in normal and perturbed states. Nat Cell Biol 2019;21:924–32.

Aragona M, Dekoninck S, Rulands S, Lenglez S, Mascré G, Simons BD, et al. Defining stem cell dynamics and migration during wound healing in mouse skin epidermis. Nat Commun 2017;8:14684.

Beard C, Hochedlinger K, Plath K, Wutz A, Jaenisch R. Efficient method to generate single-copy transgenic mice by site-specific integration in embryonic stem cells. Genesis 2006;44:23–8.

Blanpain C, Simons BD. Unravelling stem cell dynamics by lineage tracing. Nat Rev Mol Cell Biol 2013;14:489–502.

Clayton E, Doupé DP, Klein AM, Winton DJ, Simons BD, Jones PH. A single type of progenitor cell maintains normal epidermis. Nature 2007;446:185–9.

Cockburn K, Annusver K, Gonzalez DG, Ganesan S, May DP, Mesa KR, et al. Gradual differentiation uncoupled from cell cycle exit generates heterogeneity in the epidermal stem cell layer. Nat Cell Biol 2022;24:1692–700.

Dekoninck S, Hannezo E, Sifrim A, Miroshnikova YA, Aragona M, Malfait M, et al. Defining the design principles of skin epidermis postnatal growth. Cell 2020;181:604–20.e22.

Driskell RR, Giangreco A, Jensen KB, Mulder KW, Watt FM. Sox2-positive dermal papilla cells specify hair follicle type in mammalian epidermis. Development 2009;136:2815–23.

Ehrmann C, Schneider MR. Genetically modified laboratory mice with sebaceous glands abnormalities. Cell Mol Life Sci 2016;73:4623–42.

Fuchs E. Skin stem cells: rising to the surface. J Cell Biol 2008;180:273–84.

Guiu J, Hannezo E, Yui S, Demharter S, Ulyanchenko S, Maimets M, et al. Tracing the origin of adult intestinal stem cells. Nature 2019;570:107–11.

Han S, Fink J, Jörg DJ, Lee E, Yum MK, Chatzeli L, et al. Defining the identity and dynamics of adult gastric isthmus stem cells. Cell Stem Cell 2019;25:342–56.e7.

Jensen KB, Collins CA, Nascimento E, Tan DW, Frye M, Itami S, et al. Lrig1 expression defines a distinct multipotent stem cell population in mammalian epidermis. Cell Stem Cell 2009;4:427–39.

Klein AM, Simons BD. Universal patterns of stem cell fate in cycling adult tissues. Development 2011;138:3103–11.

Mascré G, Dekoninck S, Drogat B, Youssef KK, Broheé S, Sotiropoulou PA, et al. Distinct contribution of stem and progenitor cells to epidermal maintenance. Nature 2012;489:257–62.

Moad M, Hannezo E, Buczacki SJ, Wilson L, El-Sherif A, Sims D, et al. Multipotent basal stem cells, maintained in localized proximal niches, support directed long-ranging epithelial flows in human prostates. Cell Rep 2017;20:1609–22.

Morita R, Sanzen N, Sasaki H, Hayashi T, Umeda M, Yoshimura M, et al. Tracing the origin of hair follicle stem cells. Nature 2021;594:547–52.

Müller-Röver S, Handjiski B, van der Veen C, Eichmüller S, Foitzik K, McKay IA, et al. A comprehensive guide for the accurate classification of murine hair follicles in distinct hair cycle stages. J Invest Dermatol 2001;117:3–15.

Page ME, Lombard P, Ng F, Göttgens B, Jensen KB. The epidermis comprises autonomous compartments maintained by distinct stem cell populations. Cell Stem Cell 2013;13:471–82.

Piedrafita G, Kostiou V, Wabik A, Colom B, Fernandez-Antoran D, Herms A, et al. A single-progenitor model as the unifying paradigm of epidermal and esophageal epithelial maintenance in mice. Nat Commun 2020;11:1429.

Plikus MV, Mayer JA, de la Cruz D, Baker RE, Maini PK, Maxson R, et al. Cyclic dermal BMP signalling regulates stem cell activation during hair regeneration. Nature 2008;451:340–4.

Roy E, Neufeld Z, Cerone L, Wong HY, Hodgson S, Livet J, et al. Bimodal behaviour of interfollicular epidermal progenitors regulated by hair follicle position and cycling. EMBO J 2016;35:2658–70.

Sada A, Jacob F, Leung E, Wang S, White BS, Shalloway D, et al. Defining the cellular lineage hierarchy in the interfollicular epidermis of adult skin. Nat Cell Biol 2016;18:619–31.

Sánchez-Danés A, Hannezo E, Larsimont JC, Liagre M, Youssef KK, Simons BD, et al. Defining the clonal dynamics leading to mouse skin tumour initiation. Nature 2016;536:298–303.

Snippert HJ, Haegebarth A, Kasper M, Jaks V, van Es JH, Barker N, et al. Lgr6 marks stem cells in the hair follicle that generate all cell lineages of the skin. Science 2010;327:1385–9.

Teixeira VH, Nadarajan P, Graham TA, Pipinikas CP, Brown JM, Falzon M, et al. Stochastic homeostasis in human airway epithelium is achieved by neutral competition of basal cell progenitors. eLife 2013;2:e00966.

Veniaminova NA, Vagnozzi AN, Kopinke D, Do TT, Murtaugh LC, Maillard I, et al. Keratin 79 identifies a novel population of migratory epithelial cells that initiates hair canal morphogenesis and regeneration. Development 2013;140:4870–80.

Wang S, Drummond ML, Guerrero-Juarez CF, Tarapore E, MacLean AL, Stabell AR, et al. Single cell transcriptomics of human epidermis identifies basal stem cell transition states. Nat Commun 2020;11:4239.

Zouboulis CC, Picardo M, Ju Q, Kurokawa I, Törőcsik D, Bíró T, et al. Beyond acne: current aspects of sebaceous gland biology and function. Rev Endocr Metab Disord 2016;17:319–34.

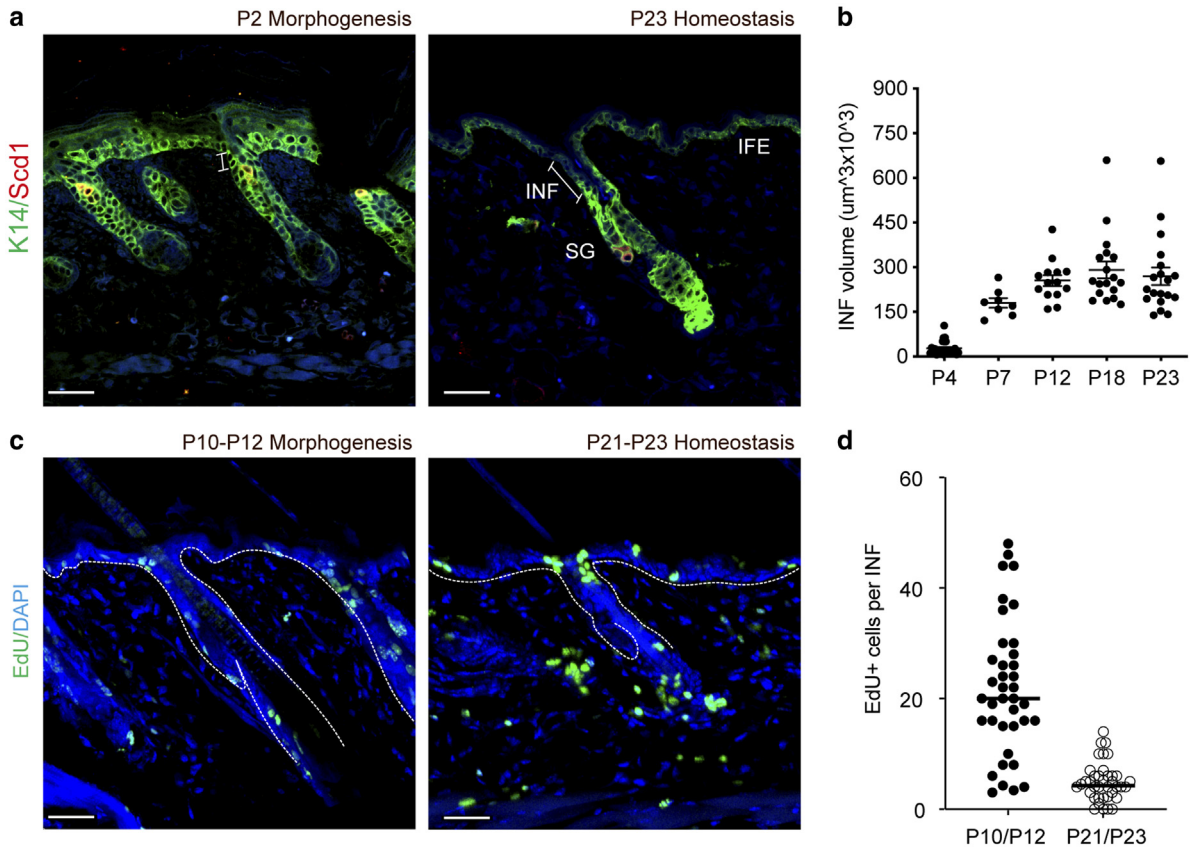

Supplementary Figure S1. Changes in volume and number of proliferating cells in the INF in morphogenesis versus homeostasis. (**a**) Representative images of rendered confocal images showing HF during morphogenesis and homeostasis stained for K14 (green) and SCD1 (red) and the strategy for the measurements of the INF volume (white brackets). (**b**) Measurements of INF volume at different developmental time points. (**c**) Representative images of rendered confocal images of EdU-positive cells during INF morphogenesis (P10, induction of EdU labeling; P12, time point of analyses) and homeostasis (P21, induction of EdU labeling; P23, time point of analyses). Shown is a quantification of the number of EdU-positive cell per INF (images described in **c**) during morphogenesis (P10/P12) and homeostasis (P21/P23). (**d**) Mice were analyzed 2 days after EdU administration. Bars = 50 μm. EdU, 5-ethynyl-2′-deoxyuridine; HF, hair follicle; INF, infundibulum; K14, keratin 14; P10, postnatal day 10; P12, postnatal day 12; P21, postnatal day 21; P23, postnatal day 23.

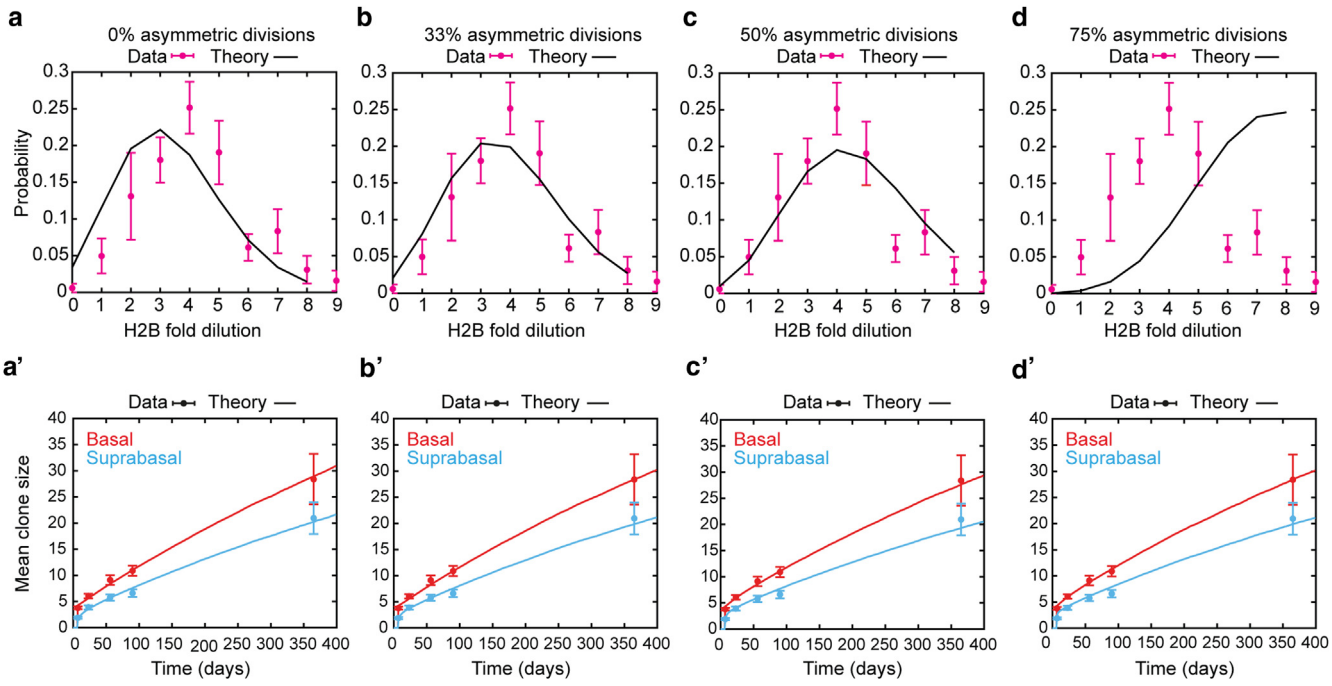

Supplementary Figure S2. Sensitivity analysis for cell cycle length and clone size and composition in INF homeostasis. (**a**–**d**) Sensitivity analysis of the model prediction for the H2B-mCherry dilution assay (top row) as well as (**a′**–**d′**) basal (red) and suprabasal (blue) mean clone size over time (bottom row) under the same conditions as top row. Lines and dots represent theory and experiments, respectively. For increasing amounts of asymmetric divisions, fitting correctly the evolution of the mean clone size requires smaller and smaller division rates. For intermediates number of asymmetric divisions (50%), we can achieve a good joint fit of both experimental measurements. INF, infundibulum.

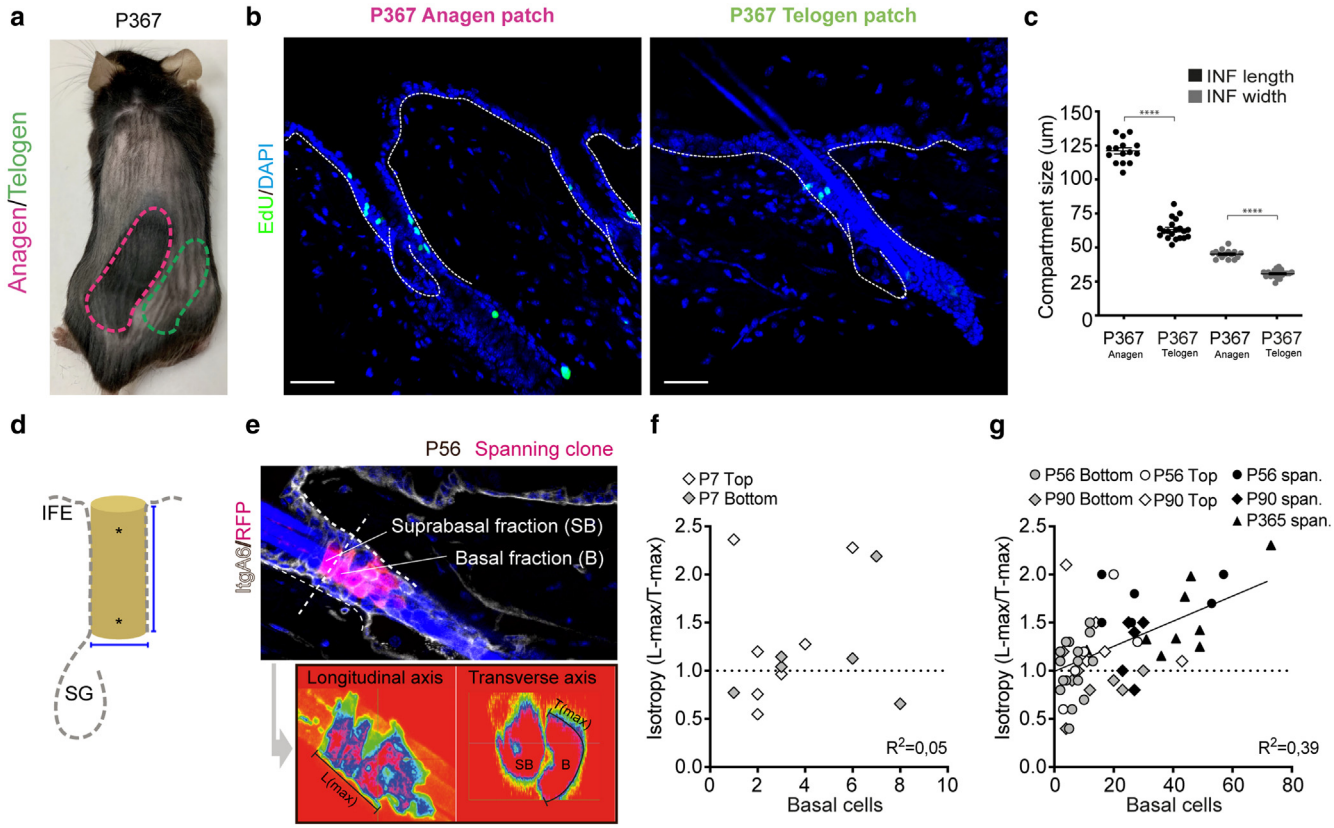

Supplementary Figure S3. Transient changes in INF cellular behavior in anagen and telogen follicles. Shown is a photograph of mice aged 1 year with asynchronous HF cycles in back skin. (**a**) Anagen areas appear darker (outlined with red line); telogen area is outlined in green. (**b**) Representative images for EdU (green) detection in anagen and telogen follicles counterstained with DAPI. (**c, d**) Measurements of INF length and width in anagen and telogen at P367 using the approach described in a schematic representation. Shown is a representative confocal image depicting a spanning RFP (red) clone. (**e**) Punctate lines outline the INF and the boundary between top and bottom subcompartments, whereas the bottom panel depicts the strategy for measuring clone isotropy. (**f**) Isotropy measurements of clones from top and bottom of the INF at P7. (**g**) Isotropy measurements of clones from top and bottom of the INF from P56, P90, and P365. Bars = 50 μm. EdU, 5-ethynyl-2′-deoxyuridine; HF, hair follicle; IFE, interfollicular epidermis; INF, infundibulum; P365, postnatal day 365; P367, postnatal day 367; P56, postnatal day 56; P7, postnatal day 7; P90, postnatal day 90.

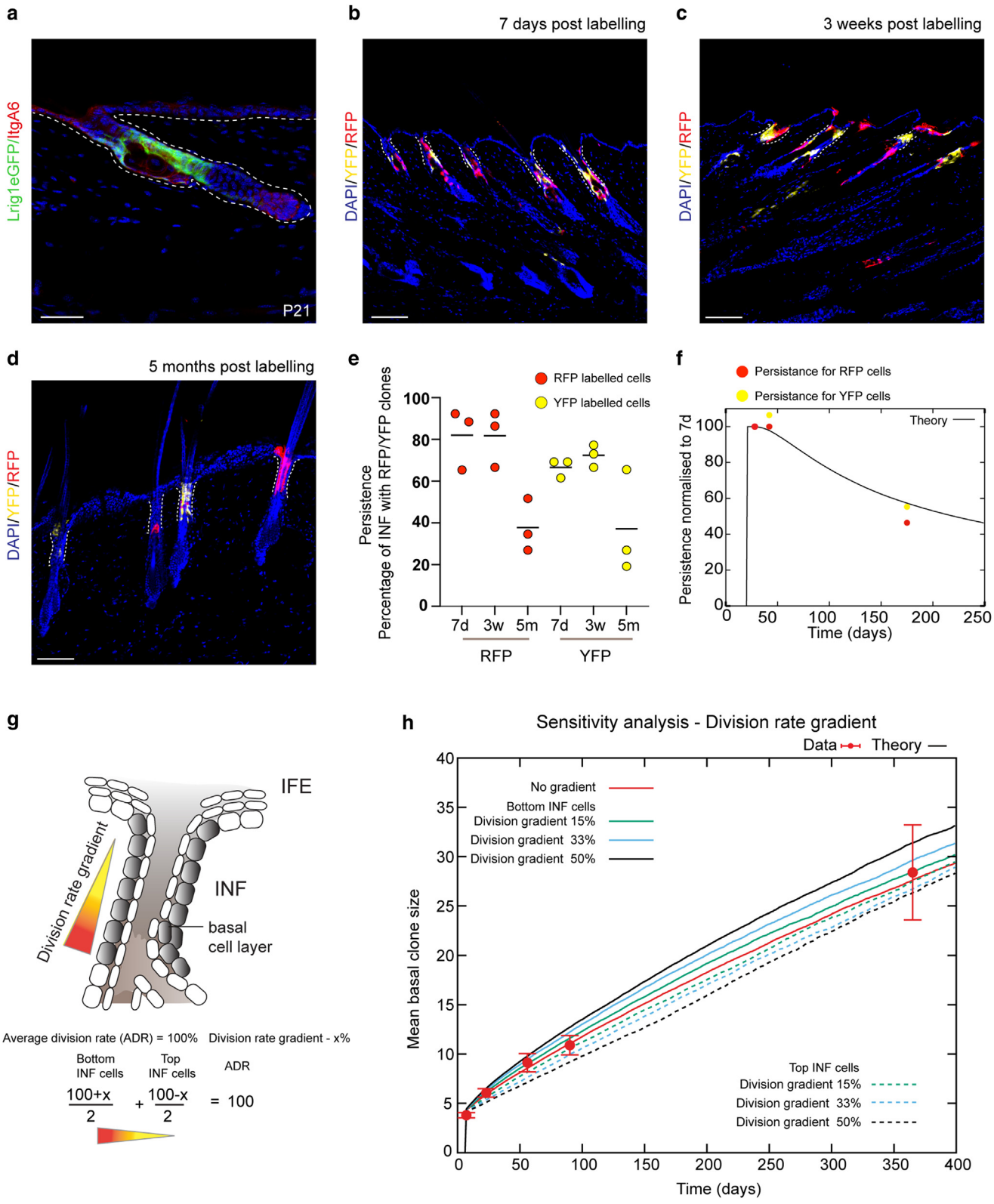

Supplementary Figure S4. Progenitor cells in the INF bottom do not outcompete progenitor cells at the top of the INF. (**a**) Representative image of *Lrig1*-eGFP expression pattern in a P21 follicle outlined with white dashed line. Bar = 50 μm. Representative confocal images of HFs (INF outlined in dotted line) with YFP/RFP-labeled cell "patches" (**b**) 7 days after labeling, (**c**) 3 weeks after labeling, and (**d**) 5 months after labeling. Bars = 100 μm. Described is the persistence of RFP- and YFP-labeled cells in the INF over time. (**e**) Lines indicate mean. (**f**) Prediction of persistence (normalized to day 7) with the same theoretical model as described in Figure 2, based on equipotency of progenitors along the INF axis (black line), provides a good fit for the observed experimental data for YFP and RFP clones (red and yellow dots). (**g**) Schematic representation of strategy employed for the modeling of division rate gradient along the INF axis. Shown is the effect of introducing a gradient in division rate along the top–down axis of the INF in the biophysical simulation. Average division rate is maintained constant, whereas the slope of the linear gradients is modified (15, 33, and 50% predictions shown in green, blue, and black, respectively [solid line for cells at the bottom

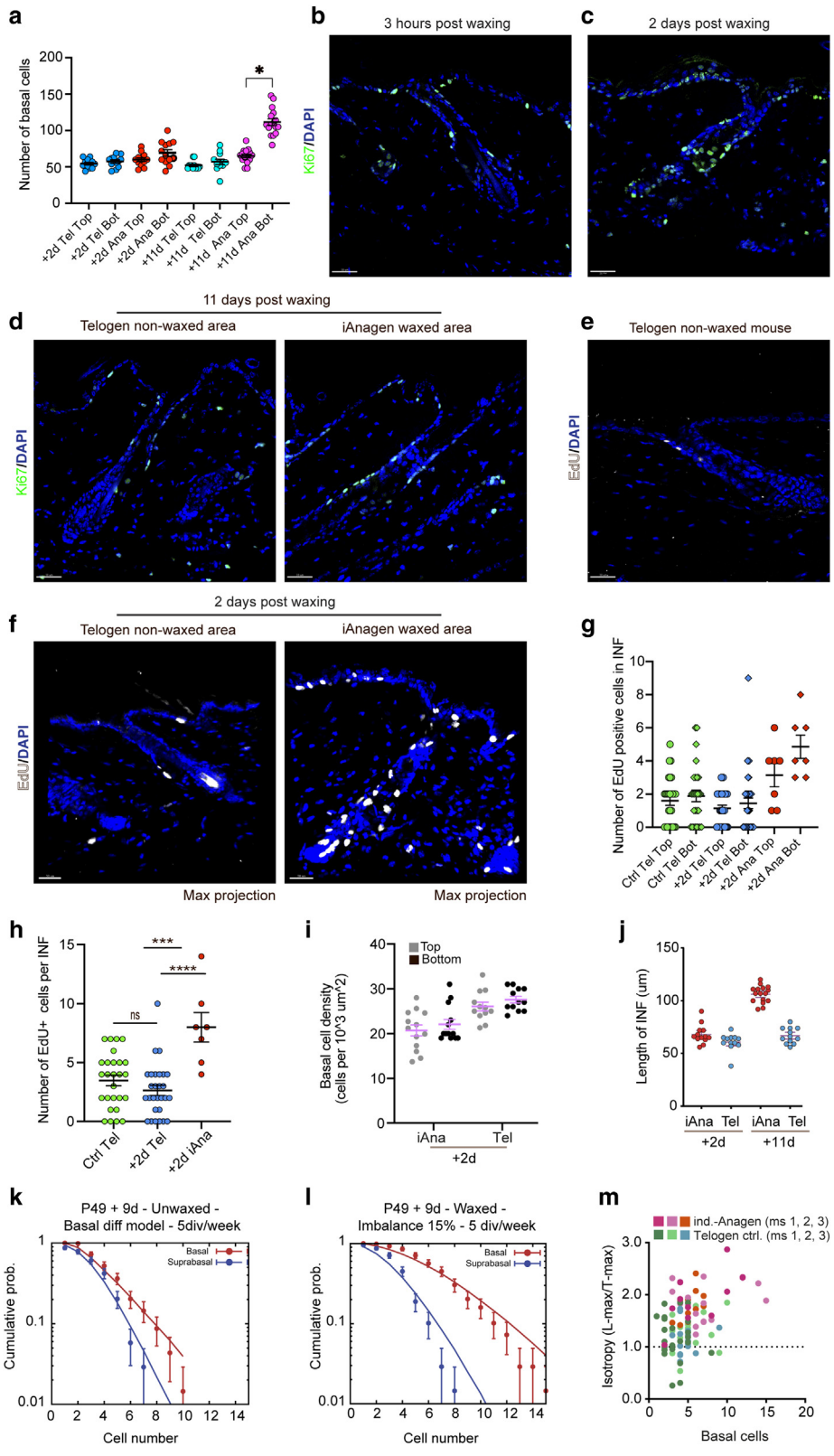

Supplementary Figure S5. Characterization of changes in the INF after induction of anagen by depilation. (**a**) Quantification of the number of basal cells in the top and bottom of the INF in mice with induced anagen areas at different time points after induction of anagen (dots represent individual measurements from 3 mice per group). (**b**–**d**) Representative confocal images of Ki-67 (green) staining in HF from areas where anagen was induced and uninduced areas that remain in telogen. (**e, f**) Representative images used for quantification of the number of EdU-positive cells per INF in telogen and iAnagen follicles. (**g**) Quantification of the number of EdU-positive cells in the top and bottom of the INF in unwaxed (Ctrl) mice as well as INF of telogen HF of unwaxed areas in mice that underwent waxing (2d tel) and INF of HFs transitioning to anagen in waxed areas of the same mice (2d anagen). Shown is the total number of EdU-positive cells per INF in the same cohort as **h**. (**i**) Measurements of basal cell density from nonwaxed (telogen, denoted as Tel) and waxed (iAnagen, denoted as iAna) INF on day 2 after depilation. (**j**) Quantification of the length of the INF in waxed (iAnagen) and unwaxed (telogen) HF on days 2 and 11 after waxing. (**k, l**) Biophysical modeling of the mean clone size (basal, red line; suprabasal, blue line) in HF in induced telogen (unwaxed) fits the evolution of the experimentally determined clone sizes (basal, red dots; suprabasal, blue dots) well in the telogen follicles with an estimated division rate of 5 divisions a week, whereas the clone size in the induced anagen follicles has a good fit if the model is adjusted to a 15% increase in the production of basal cells. (**m**) Measurements of INF clone isotropy in iAnagen and telogen follicles. Bars = 30 μm. All error bars indicate SEM. Ctrl, control; EdU, 5-ethynyl-2′-deoxyuridine; HF, hair follicle; INF, infundibulum.

of INF and punctate line of the same color for cells at the top of the INF from the same conditions], which are similar to the previous model without gradient in red). Note that in this model, self-renewal only expels nearest neighbors, so that cells locally compete with neighbors with very similar properties, which does not produce significant flows of cells from bottom to top. **(h)** Error bars indicate SEM. HF, hair follicle; IFE, interfollicular epidermis; INF, infundibulum; P21, postnatal day 21.